12-25-2009

Double Superhelix Model of High Density Lipoprotein

Zhiping Wu
Cleveland Clinic

Valentin Gogonea
Cleveland State University, V.GOGONEA@csuohio.edu

Xavier Lee
Cleveland Clinic

Mathew A. Wagner
Cleveland Clinic

THE JOURNAL OF BIOLOGICAL CHEMISTRY VOL. 284, NO. 52, pp. 36605–36619, December 25, 2009

Double Superhelix Model of High Density Lipoprotein*[S]

Received for publication, June 30, 2009, and in revised form, September 10, 2009 Published, JBC Papers in Press, October 7, 2009, DOI 10.1074/jbc.M109.039537

Zhiping Wu[‡§], Valentin Gogonea[‡¶], Xavier Lee[‡§], Matthew A. Wagner[‡§], Xin-Min Li[‡§], Ying Huang[‡§], Arundhati Undurti[‡§], Roland P. May[‖], Michael Haertlein[‖], Martine Moulin[‖], Irina Gutsche[**], Giuseppe Zaccai[‖‡‡], Joseph A. DiDonato[‡§], and Stanley L. Hazen[‡§§§1]

From the [‡]Department of Cell Biology, [§]Center for Cardiovascular Diagnostics and Prevention, and [§§]Department of Cardiovascular Medicine, Cleveland Clinic, Cleveland, Ohio 44195, the [¶]Department of Chemistry, Cleveland State University, Cleveland, Ohio 44115, [‖]Institut Laue-Langevin, 6 Rue Jules Horowitz, BP 156, 38042 Grenoble Cedex 9, France, [**]Unit of Virus-Host Interaction, Unité Mixte de Recherche 5233 Université Joseph Fourier-European Molecular Biology Laboratory-CNRS, 6 Rue Jules Horowitz, BP 181, 38042 Grenoble Cedex 9, France, and [‡‡]Institut de Biologie Structurale, Commissariat à l'Energie Atomique-CNRS-Université Joseph Fourier, 38027 Grenoble, France

High density lipoprotein (HDL), the carrier of so-called "good" cholesterol, serves as the major athero-protective lipoprotein and has emerged as a key therapeutic target for cardiovascular disease. We applied small angle neutron scattering (SANS) with contrast variation and selective isotopic deuteration to the study of nascent HDL to obtain the low resolution structure in solution of the overall time-averaged conformation of apolipoprotein AI (apoA-I) *versus* the lipid (acyl chain) core of the particle. Remarkably, apoA-I is observed to possess an open helical shape that wraps around a central ellipsoidal lipid phase. Using the low resolution SANS shapes of the protein and lipid core as scaffolding, an all-atom computational model for the protein and lipid components of nascent HDL was developed by integrating complementary structural data from hydrogen/deuterium exchange mass spectrometry and previously published constraints from multiple biophysical techniques. Both SANS data and the new computational model, the double superhelix model, suggest an unexpected structural arrangement of protein and lipids of nascent HDL, an anti-parallel double superhelix wrapped around an ellipsoidal lipid phase. The protein and lipid organization in nascent HDL envisages a potential generalized mechanism for lipoprotein biogenesis and remodeling, biological processes critical to sterol and lipid transport, organismal energy metabolism, and innate immunity.

High density lipoprotein (HDL)[2] functions in removal of cholesterol from peripheral tissues, such as within the artery wall, for delivery to the liver and ultimate excretion as biliary cholesterol within the intestinal lumen, a process called reverse cholesterol transport (1, 2). Plasma levels of HDL cholesterol and apolipoprotein AI (apoA-I), the major protein component of HDL, are inversely related to the risk of developing coronary artery disease (3–5). Moreover, genetic alterations that induce changes in apoA-I levels in both animals and humans alter susceptibility for development of atherosclerotic heart disease (3–6). Thus, numerous interventions aimed at enhancing reverse cholesterol transport are being examined as potential novel therapeutic interventions for the prevention and treatment of cardiovascular disease (7, 8). Examples include methods for generating new HDL particles through enhanced production or delivery of either intact apoA-I (9, 10) or peptide mimetics of apoA-I (11), as well as modulating interactions between nascent HDL and proteins involved in HDL particle maturation and remodeling for potential therapeutic benefit (12–14). Structural elucidation often serves as the "Rosetta Stone" for enhanced understanding of function. It is thus remarkable that despite its importance to numerous biological and biomedical functions and its current prominent role as a target for therapeutic interventions, to date, the structures of neither the protein nor lipid components of nascent HDL have been directly visualized, and the high resolution structure of the particle remains unknown.

In the absence of high resolution structures, numerous models of nascent HDL have been proposed (recently reviewed in Refs. 15, 16). In general, these have relied on various biophysical and biochemical studies and are named after the proposed overall architecture of apoA-I within the particle (*e.g.* picket fence model (17), double belt model (18, 19), various hairpin loop models (20–22), and most recently, the solar flares model (23)). Each of these models of nascent HDL assumes a structure composed of a central phospholipid and cholesterol bilayer with amphipathic α-helical apoA-I arranged around the perimeter of the central lipid core. Refinement of the protein orientation has been dictated by biophysically determined constraints such as hydrophobic/hydrophilic character along the

* This work was supported, in whole or in part, by National Institutes of Health Grants P01 HL076491-055328, P01 HL077107-050004, P01 HL087018-02001, and 1R15 GM070469-01. This work was also supported by Case Western Reserve University/Cleveland Clinic Clinical and Translational Science Award 1KL2RR024990.

[S] The on-line version of this article (available at http://www.jbc.org) contains supplemental Experimental Procedures, Figs. S1–S11, Tables S1–S7, and additional references.

The double superhelix model (PM0075984) reported in this paper has been deposited in the Protein Model Database (http://mi.caspur.it/PMDB).

[1] To whom correspondence should be addressed: Cleveland Clinic, 9500 Euclid Ave., NE-10, Cleveland, OH 44195. Tel.: 216-445-9763; Fax: 216-636-0392; E-mail: hazens@ccf.org.

[2] The abbreviations used are: HDL, high density lipoprotein; SANS, small angle neutron scattering; HD-MS/MS, hydrogen/deuterium exchange tandem mass spectrometry; H/D, hydrogen/deuterium; HUVEC, human umbilical vein endothelial cell; PBS, phosphate-buffered saline; POPC, 1-palmitoyl-2-oleoyl-*sn*-glycero-3-phosphocholine; LCAT, lecithin cholesterol acyltransferase; SR-BI, scavenger receptor class B, type I; rHDL, recombinant HDL; rrHDL, reconstituted recombinant HDL.

predicted α-helices, overall α-helical content as estimated by circular dichroism, measured distance constraints between inter- and intra-chain amino acids by multiple approaches, and more recently, quantitative indices of solvent accessibility and dynamics as determined by amide bond hydrogen/deuterium exchange throughout the apoA-I polypeptide backbone. Although all current models share an anti-parallel orientation of two apoA-I predominantly α-helical chains, the overall conformation of the apoA-I α-helical chains within the particle is still debated. Of note, none of the models is based upon studies that provide direct imaging of the shape of apoA-I or the lipid core within nascent HDL in solution.

Structural data from individual low resolution platforms can have limited usefulness in resolving the molecular structure of biological compounds, but limitations in structural definition inherent in individual low resolution biophysical approaches can be partially overcome by combining them synergistically (24–26). Indeed, it is becoming increasingly recognized within the structural biology field that merging multiple complementary techniques can prove particularly valuable when only low resolution structures are available. For example, Fleishman *et al.* (27) have recently shown how combining multiple biophysical/biochemical constraints and computational analyses coupled with cryo-EM low resolution data can result in enhanced resolution, as well as provide mechanistic understanding of membrane protein structure and function without crystallographic data.

Herein, we develop and apply to the study of nascent HDL a broadly applicable, multidisciplinary methodological platform for investigating the solution structure of macromolecular complexes resistant to traditional structural approaches. By uniting the diverse yet synergistic nonperturbing experimental techniques of small angle neutron scattering (SANS) with contrast variation, isotopic deuteration of selected macromolecule components, and hydrogen/deuterium exchange tandem mass spectrometry (HD-MS/MS), we have been able to describe the time-averaged conformation of protein and lipid components of nascent HDL separately at low resolution and then to enhance the resolution of these shapes by incorporating multiple additional biophysical constraints to build a computational model for the particle.

EXPERIMENTAL PROCEDURES

Preparation of Nascent HDL—The particle composition selected for our studies, the methods for particle generation, and the functional characterizations performed to demonstrate a biologically active particle closely align with the current HDL-based therapeutic interventions being evaluated in the clinic (28–30) and nascent HDL produced by macrophages (31).

Human apoA-I was isolated from plasma of healthy volunteers. Briefly, human HDL was isolated from a pool of fresh plasma by ultracentrifugation adjusted with KBr to a density range of 1.07–1.21 g/ml as described. Lipid-free human apoA-I was prepared by delipidation of isolated human HDL using methanol:ether:chloroform followed by ion exchange chromatography (32). The purity of isolated human apoA-I was verified by SDS-PAGE. Recombinant human apoA-I was generated in *Escherichia coli* and isolated as described previously (33). To prepare deuterated recombinant human apoA-I, the kanamycin-resistant plasmid pET20b$^+$ encoding His_6-tagged human apoA-I was transformed into *E. coli* BL21(DE3) cells. Kanamycin resistance allows efficient selection and maintenance of the expression construct under high cell density growth conditions required in deuterated minimal media (34–36). Cells were grown in 85% deuterated minimal medium (85% D_2O), 15% H_2O, 6.86 g/liter $(NH_4)_2SO_4$, 1.56 g/liter KH_2PO_4, 6.48 g/liter $Na_2HPO_4{\cdot}2H_2O$, 0.49 g/liter diammonium hydrogen citrate, 0.25 g/liter $MgSO_4{\cdot}7H_2O$, 1.0 ml/liter (0.5 g/liter $CaCl_2{\cdot}2H_2O$, 16.7 g/liter $FeCl_3{\cdot}6H_2O$, 0.18 g/liter $ZnSO_4{\cdot}7H_2O$, 0.16 g/liter $CuSO_4{\cdot}5H_2O$, 0.15 g/liter $MnSO_4{\cdot}4H_2O$, 0.18 g/liter $CoCl_2{\cdot}6H_2O$, 20.1 g/liter EDTA), 40 mg/liter kanamycin with hydrogenated glycerol as carbon source (5 g/liter). Deuterated apoA-I was purified by nickel affinity chromatography using established methods (23, 33).

Reconstituted nascent HDL was prepared using the modified sodium cholate dialysis method (37) at an initial molar ratio of 100:10:1 of POPC:cholesterol:isolated apoA-I, which is a modification of the original seminal studies by Matz and Jonas (32) who first reported the cholate dialysis method for reconstituted HDL preparation. HDL particles were further purified by gel filtration chromatography using a Sephacryl S300 column (GE Healthcare). The size of reconstituted nascent HDL was routinely measured as described previously using dynamic light scattering and nondenaturing PAGE (23). The stoichiometry of all nascent HDL preparations was determined as described previously (23). The amount of sodium cholate remaining in all reconstituted nascent HDL preparations was quantified by high pressure liquid chromatography tandem mass spectrometry to confirm no significant residual cholate was present. The stoichiometry of apoA-I on nascent HDL made of human plasma isolated apoA-I (rHDL) and bacterially produced recombinant His-tagged apoA-I (rrHDL) were determined by chemical cross-linking studies as described previously (23).

HDL Characterization by Circular Dichroism Spectroscopy—Far-UV circular dichroism spectra were recorded on an 815 CD spectrophotometer (Jasco). Reconstituted nascent HDL samples (rHDL and rrHDL) were analyzed at ambient temperature in continuous scan mode with a 1-nm bandwidth at a wavelength of 260 to 185 nm and with a path length of 1 mm. The spectra were normalized to mean residue ellipticity with the use of a mean residue molecular mass of 115.4 Da for apoA-I. Fractional α-helix contents were calculated using the neural network-based K2d program (38).

HDL Characterized by Lecithin Cholesterol Acyltransferase (LCAT) Activity Assay and LCAT Binding—The activation of LCAT by rHDL and rrHDL with trace amounts of [^{3}H]cholesterol added was measured as described before with slight modification (23). The reaction complex contained 0–35 μM cholesterol in a final concentration of 10 mM phosphate (pH 7.4), 1 mM EDTA, 150 mM NaCl, 2 mM β-mercaptoethanol, 0.6% fatty acid-free bovine serum albumin, and 20 ng of purified His_6-tagged human LCAT (recombinant human LCAT). The reactions were carried out in triplicate at 37 °C for 35 min under argon. LCAT activity was determined by calculating the conversion efficiency of [^{3}H]cholesterol to [^{3}H]cholesteryl ester

after lipid extraction of reaction mixture followed by thin layer chromatography (23).

Measurements of apparent dissociation constants between LCAT and both rHDL and rrHDL were performed using a BIAcore 3000 SPR Biosensor (BIAcore) following the methods of Jin *et al.* (39) with modifications. Briefly, ~8000 resonance units of polyclonal antibody against apoA-I (Biodesign) was immobilized on a CM5 sensor chip through primary amino groups using reactive esters. Nascent HDLs were captured on the sensor chip through interaction with antibody against apoA-I by injecting 7 μM HDL at a flow rate of 15 μl/min in 10 mM PBS buffer (pH 7.4) into the flow cell. To determine the K_d values between recombinant human LCAT and nascent HDL, recombinant human LCATs ranging from 500 to 2000 nM were prepared in binding buffers of 10 mM PBS (pH 7.4) and injected over the surface of the sensor chip at a flow rate of 20 μl/min. At the end of each cycle, surfaces of the sensor chips were regenerated by injection of 15 mM HCl at the same flow rate. The apparent dissociation constants were obtained by fitting background-subtracted SPR binding data to the 1:1 binding with drifting base-line model using the BIAevaluation software version 4.0.

HDL Characterized by Cholesterol Efflux Assay—Subconfluent J774A.1 murine macrophage cells in 48-well plates were loaded by 0.3 μCi/ml [^{3}H]cholesterol overnight in 0.4 ml of DGGB (Dulbecco's modified Eagle's medium supplemented with 50 mM glucose, 2 mM glutamine, and 0.2% bovine serum albumin). The day after cholesterol was loaded, the cells were washed three times in PBS and treated with or without various 5 μg/ml HDLs for 6 h in serum-free Dulbecco's modified Eagle's medium. The radioactivity in the chase media was determined after brief centrifugation to remove pellet debris. Radioactivity in the cells was determined by extraction in hexane: isopropyl alcohol (3:2, v/v) with the solvent evaporated in a scintillation vial prior to counting. The percent cholesterol efflux was calculated by radioactivity in the medium divided by the total radioactivity (medium radioactivity plus cell radioactivity) (33).

SR-BI-specific Binding of HDL—rHDL was iodinated using Bolton-Hunter reagent to prevent oxidation of the particle (40). 293-T cells were transfected with vector or SR-BI using Lipofectamine-2000 according to the manufacturer's instructions. The next day, cells were plated in 24-well plates, and after another 24 h, specific binding of the radiolabeled rHDL to SR-BI was determined by incubating ^{125}I-rHDL with either vector-transfected or SR-BI-transfected cells for 1.5 h at 4 °C. After 1.5 h, cells were washed twice with 250 mM NaCl, 25 mM Tris (pH 7.4) and once with 250 mM NaCl, 25 mM Tris (pH 7.4) with 2 mg/ml bovine serum albumin. Cells were solubilized in 1 ml of 0.1 M NaOH at room temperature for 20 min, and cell-associated radioactivity was subsequently determined with a Gamma4000 spectrometer (Beckman Coulter, Fullerton, CA). Specific binding was calculated as total binding minus binding in the presence of a 30-fold excess of unlabeled rHDL. For the competition assay, a 30-fold excess of either unlabeled human HDL from plasma, unlabeled reconstituted HDL prepared with recombinant apoA-I (rrHDL), or unlabeled POPC small unilamellar vesicles was added along with 100 μg/ml iodinated human HDL to determine inhibition of iodinated human HDL binding to SR-BI (41).

Measurement of Anti-apoptotic Activity of HDL—Human umbilical vein endothelial cells (HUVEC) were plated overnight in 60-mm dishes in MCDB media supplemented with 15% fetal bovine serum. The next day, cells were washed with PBS, and serum was deprived for 6 h with simultaneous incubation with either 500 μg/ml pHDL, 500 μg/ml rHDL, 500 μg/ml apoA-I, or 500 μg/ml small unilamellar vesicles generated with POPC. After 6 h, apoptosis was measured using an annexin V-fluorescein isothiocyanate apoptosis detection kit (Pharmingen). Briefly, cells were washed twice with PBS, harvested, and suspended in 1× binding buffer (10 mM Hepes/NaOH (pH 7.4), 140 mM NaCl, 2.5 mM $CaCl_2$) at a concentration of 10^6 cells/ml. The solution was transferred to a 5-ml culture tube and incubated with annexin and propidium iodide for 15 min at room temperature in the dark according to the manufacturer's instructions. Flow cytometry of labeled cells was performed on a FACScan (BD Biosciences).

Determination of Surface VCAM-1 Protein—HUVEC were plated overnight in 96-well plates in MCDB-105 media supplemented with 15% fetal bovine serum. The next day, cells were washed twice with PBS (pH 7.4) and preincubated with either 500 μg/ml pHDL, 500 μg/ml rHDL, 500 μg/ml apoA-I, or 500 μg/ml POPC small unilamellar vesicles for 2 h. After 2 h, 5 ng/ml of tumor necrosis factor-α was added, and cells were incubated for an additional 6 h. Cells were then washed three times with PBS (pH 7.4) and fixed in 4% paraformaldehyde for 30 min on ice. Cells were subsequently washed and blocked overnight with 5% bovine serum albumin. The day after blocking, cells were incubated with anti-VCAM-1 primary antibody (sc-53778, Santa Cruz Biotechnology) for 2 h at room temperature. After three washes with PBS (pH 7.4), cells were incubated with sheep anti-mouse horseradish peroxidase-conjugated secondary antibody (GE Healthcare) for 2 h at room temperature. 3,3′,5,5′-Tetramethylbenzidine substrate was subsequently added to each well and the reaction stopped after 20 min by addition of 1 M HCl. Absorbance was recorded at 450 nm on a 96-well plate reader (Spectramax 384 Plus, Molecular Devices, Sunnyvale, CA).

SANS Experiment—Small angle neutron scattering experiments were carried out at the instrument D22 of the Institut Laue-Langevin, Grenoble, France. D22 is a classical pinhole camera that provides the highest neutron flux among all comparable SANS instruments in existence (42). Data collected from two positions of the detector (2 and 5.6 m with collimation lengths of 2.8 and 5.6 m) covered the momentum transfer (q) range from 0.008 to 0.35 Å^{-1}. q is defined as $2\pi(\sin\theta)/\lambda$, where 2θ is the scattering angle. The wavelength λ of the neutron beam used was 6 Å. Data beyond 0.25 Å^{-1} were too noisy to analyze.

To understand the organization of the protein and lipid in HDL contrast variation ($[D_2O]/[H_2O + D_2O]$ ratio) was required. The HDL samples were measured in 0, 12, 42, and 90% D_2O solution to ensure the required levels of contrast. From the corresponding scattering curves, two important parameters were obtained for each contrast as follows: the radius of gyration (R_g) and the intensity at 0 angle $I(q = 0)$. R_g

values were obtained based on the Guinier approximation (43), which is valid for q values $(R_g q)^2 < 1$ (Equation 1).

$$\lim_{q \to 0} I_{corr}(q) = I(0)\exp(-R_R^2 q^2/3) \quad \text{(Eq. 1)}$$

The logarithmic intensities varied linearly with q^2 in the chosen Guinier range and the obtained R_g were stable against slight change in q range. The molecular mass (M) of the HDL particle was calculated as 200,000 Da based on the absolute scale measured $I(q = 0)$ (Equation 2), in which C (mg/cm^3) is the concentration of HDL, $\sum b$ (cm) is the particle scattering length, V (cm^3) is the particle volume, ρ^0 (cm^{-2}) is the solvent scattering length density, and N_A is Avogadro's number; the term in brackets is the particle excess scattering length normalized to unit molecular mass (44). The molecular mass calculated from the data corresponded to one HDL particle.

$$I(0)/C = N_A((\sum b - p^0 V)/M)^2 M \quad \text{(Eq. 2)}$$

The program DAMMIN (45), a simulated annealing method, was used to calculate a low resolution model of the lipid core from the scattering curve of the sample in 42% D_2O. Likewise, the 12% scattering curve was used for the modeling of the protein. In the approach, the starting structure is a sphere of diameter equal to the maximum particle dimension, which was estimated from the scattering curve, via the distance distribution function $P(r)$. The sphere was filled with dummy atoms with their size determined by the highest value of momentum transfer (q) of the scattering curve. To enhance the signal to noise ratio of the sample in 12% D_2O, deuterated apoA-I was used for the reconstitution of the HDL particle. The χ value of the simulated annealing modeling for lipid is less than 1 and 5.2 for the protein. Both are in the excellent or reasonable range of statistics.

SAXS Experiment—Small angle x-ray scattering data of nascent HDL in solution were collected at the X33 beamline (DESY, Hamburg, Germany) at particle concentrations ranging from 2 to 16.0 mg/ml. At a sample detector distance of 2.7 m, the range of momentum transfer $0.01 < q < 0.5$ Å^{-1} was covered ($\lambda = 0.15$ nm the x-ray wavelength). The data were processed with program PRIMUS (46) using standard procedures. The forward scattering intensity $I(q = 0)$ and the radius of gyration (R_g) were evaluated with program AUTORG (47) using the Guinier approximation. The effective molecular mass of the solute was estimated by comparison of the forward scattering intensity with that from reference solutions of bovine serum albumin (molecular mass = 66 kDa).

Electron Microscopy Studies—Negatively stained HDL was obtained by applying a diluted solution of HDL particles (<0.2 mg of protein/ml) to the clear side of carbon on a carbon-mica interface and stained with 2% (w/v) uranyl acetate. Images were recorded under low dose conditions with a JEOL 1200 EX II microscope at 100 kV. Selected negatives were then digitized on a Zeiss scanner (Photoscan TD) at a step size of 14 μm giving a pixel size of 3.5 Å at the specimen level. Subsequent data processing was performed with the Imagic package. The data set, centered by translation, was subjected to multivariate statistical analysis and classification.

Computational Modeling of Nascent HDL—An all-atom computational model of nascent HDL was constructed by combining modeling techniques with experimental data, including contrast variation SANS, HD-MS/MS data, and reported distance constraints from cross-linking, fluorescence resonance energy transfer, and electron spin resonance experiments (20, 21, 48, 49). The overall strategy in constructing a model of nascent HDL was to use the SANS low resolution structures obtained by deconvoluting the experimental SANS curves of 12 and 42% D_2O as scaffolds to build molecular models for the protein and lipid components of nascent HDL, respectively. The overall model building involved over 250 iterative steps (*i.e.* over 250 models created for nascent HDL) with assessments of the goodness of fit with both SANS curves and experimentally determined H/D exchange data at every step. At each refinement step, precedence was always placed on SANS data for global conformation, whereas more fine-tuned refinements of local architecture primarily utilized H/D exchange data. It is worth noting that hydrogen/deuterium exchange, in conjunction with NMR and/or tandem mass spectrometry analysis (50, 51), has been used extensively in the past to determine the local environment, such as solvent accessibility and dynamics, of amino acid residues in proteins or in macromolecular complexes involving proteins. Determination of H/D exchange through either NMR or mass spectrometry methodology provides constraints that can help aide in structural modeling because amide hydrogen H/D exchange rates (and their degree of protection) are sensitive to the local environment of amino acid residues in various protein secondary structures (α-helix, β-pleated sheets, etc.). The degree of H/D exchange in amide backbone hydrogen atoms depends upon both solvent accessibility and local interactions (*e.g.* participation in hydrogen bonds in α-helical sites, hydrophobic contacts, and protein dynamics).

An iterative co-refinement process was performed for each contrast variation study to first develop an overall model of the protein component based upon SANS and HD-MS/MS data, then the lipid core, followed by a combined model with energy minimization at every step. A starting model for the lipoprotein was constructed using MODELER, PyMOL, and Swiss-PDB-Viewer programs (52, 53), by arranging the apoA-I chains into an anti-parallel superhelical conformation to match the 12% D_2O SANS low resolution structure. The crude protein model obtained in this way was further refined by iteratively adjusting the shape and the degree of protection of amide hydrogen for exchange. As described in detail in the supplemental material, the program DEXANAL (23) was used to determine per residue deuterium incorporation factors (D_0^i), residue unfolding constants (K_u^i), and H/D exchange rate constants (k_{xc}^i) from the experimental H/D exchange data of overlapping peptic peptides. DEXANAL was also employed to calculate per residue H/D exchange probabilities (XP_i) from three-dimensional molecular models. In this manner, an iterative co-refinement approach was used to improve the computational model so that predicted SANS and H/D exchange data matched experimental SANS and HD-MS/MS data. Use of DEXANAL for incorporating H/D exchange data into molecular models was validated using proteins with known crystallographic structure and published H/D exchange data as outlined in detail in supplemental Figs. S1 and S2 and Tables S1–S4.

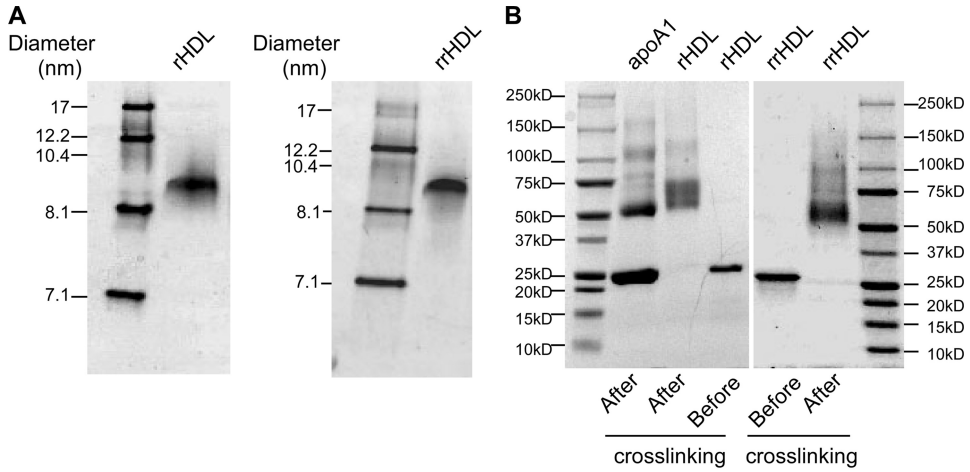

C

Stoichiometry of reconstituted nascent HDL

	POPC	Cholesterol	ApoA1	Cholate
Theoretical	100	10	1	0
Measured (rHDL)	89.3±4.8	9.7 ± 0.5	1	<0.01
Measured (rrHDL)	105 ± 1	7.4 ± 0.4	1	<0.01

D

Size of reconstituted nascent HDL

	rHDL Diameter	rrHDL Diameter
ND-PAGE	96 ± 1 Å	96 ± 1 Å
Light-scattering	110 ± 1 Å	113 ± 2 Å

FIGURE 1. **Characterization of reconstituted nascent HDL particles.** Nascent HDL particles were prepared using a modified cholate dialysis method at a molar ratio of 100:10:1, POPC:cholesterol:apoA-I (76). Before being used in structural analyses, HDL particles were characterized by a variety of biological, biochemical, and biophysical methods. *A*, nondenaturing gel analyses of reconstituted nascent HDL containing purified human apoA-I from healthy donors (*rHDL*, *left panel*) and reconstituted nascent HDL containing recombinant human apoA-I purified from *E. coli* (*rrHDL*, *right panel*). Purified nascent HDL by gel filtration (10 μg of protein) was loaded on a 4–20% gradient gel. The purity of the nascent HDL preparation was confirmed by ND-PAGE analysis. *B*, SDS-polyacrylamide gel analyses of cross-linked apoA-I within rHDL and rrHDL particles. After cross-linking, a broad band was shown at about the 50–70-kDa position, indicating each HDL particle contains two apoA-I molecules. The broadened band pattern is consistent with prior reports for an apoA-I dimer in similarly cross-linked HDL (20, 37). *C*, stoichiometry of reconstituted HDL. The chemical composition of HDL particles was determined using a variety of methods. *D*, size of nascent HDL particles was determined both by comparison with the known diameter of globular standard proteins and by light scattering spectroscopy (23). The results represent an average ± S.D. of three measurements.

The neutron scattering curves of the models of apoA-I within nascent HDL were computed using a modification of the SASSIM program (54). Instrument smearing was taken into account in calculating the scattering intensity as described in Merzel and Smith (54), and the relative wavelength spread of neutrons ($\Delta\lambda/\lambda$) used was 0.1 as suggested by Svergun *et al.* (55). At each refinement step, the model was energy-minimized using the OPLS force field (56) (using the GROMACS program (57)).

The lipid phase (200 POPC molecules and 20 cholesterol molecules) was modeled to follow the helical orientation of protein hydrophobic surface filling the inside groove, and overall fits the experimentally visualized SANS prolate ellipsoid obtained by deconvoluting the 42% D_2O scattering curve. The lipid model was refined further by performing energy minimization of the whole particle and by matching its calculated scattering intensity curve to the experimentally obtained one (42% D_2O). Additional model refinement using experimental geometrical constraints such as chemical cross-links, fluorescence resonance energy transfer, and electron spin resonance distances are described in detail in the supplemental material.

RESULTS

Small Angle Neutron Scattering of Nascent HDL—Small angle scattering is a powerful approach for structural studies of macromolecules in solution. It provides a low resolution structure and is particularly useful in revealing details of the organization of a multicomponent system. For example, in a contrast variation experiment of SANS, D_2O/H_2O levels are varied such that the scattering length density of the solvent is adjusted to match that of a component within a complex (*e.g.* protein, lipid, DNA, or RNA), essentially rendering that component invisible (58). Thus, SANS can link structural and compositional information in solution in a way that is difficult to attain by other approaches. Indeed, SANS with contrast variation was the first method to correctly predict the structural orientation of protein and DNA within the fundamental subunit of chromatin, the nucleosome (59), as well as to triangulate the location of various proteins and RNA within the ribosome (60–62), the intracellular complex that translates the genetic code into proteins.

To probe the structure of apoA-I within nascent HDL particles, we examined reconstituted nascent HDL particles produced using human apoA-I as described under "Experimental Procedures." Dynamic light scattering, biochemical, and cross-linking/mass spectrometry analyses of HDL indicated monodispersed preparations with two apoA-I molecules per particle, and overall stoichiometry of apoA-I:phospholipid:cholesterol of ~1:100:10 (mol/mol; see Fig. 1). Prepared nascent HDL particles for structural studies were confirmed to be biologically functional with respect to a broad array of reported HDL activities, including cholesterol efflux from cholesterol-loaded macrophages, LCAT binding, activity, and catalytic efficiency, specific binding to the HDL receptor SR-BI, anti-apoptotic activity, and anti-inflammatory activity (Figs. 2 and 3). Absolute scale SANS analysis confirmed the predominance of a 200,000-Da lipoprotein particle in solution corresponding to the monomer of nascent HDL containing two apoA-I per particle. To obtain information about the shape of apoA-I within HDL, scattering intensity data were collected in 12% D_2O. At this concentration of D_2O, the scattering length density of sol-

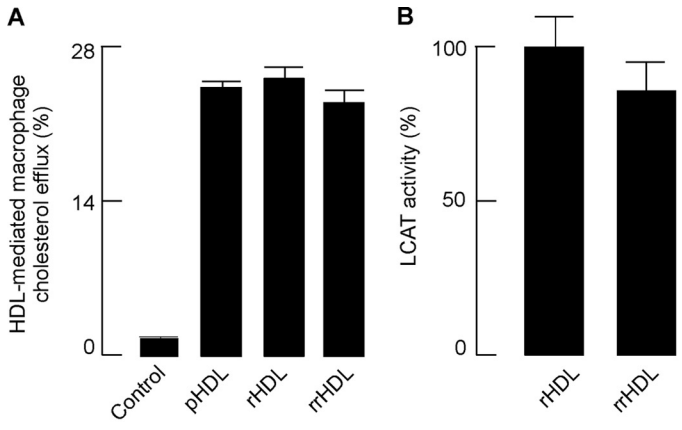

C

Dissociation constants of human recombinant LCAT binding to rHDL and rrHDL by surface plasmon resonance

	rHDL	rrHDL
K_d (μM)	0.9	1.4

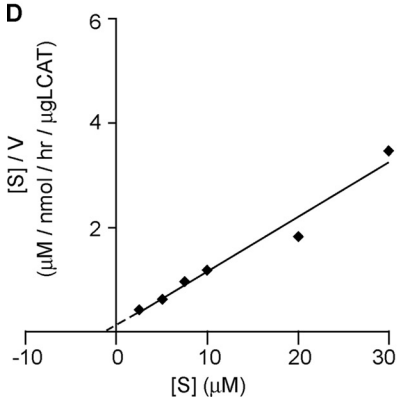

Reaction Kinetics of HDL Particles with LCAT

	Apparent K_m	Apparent V_{max}	Apparent V_{max}/K_m
	μM	nmol CE/hr/μg	nmol CE/hr /μg/μM
rrHDL	1.0 ± 0.4	9.5 ± 1.0	11.2 ± 4.5
rrHDL[a]	1.0 ± 0.2	—	—
rHDL[b]	1.7 ± 0.3	20.5 ± 0.9	12.1

a, Alexander ET et al., 2005 Biochemistry
b, Chisholm JW, et al., 1999 Journal of Lipid Research

FIGURE 2. **Cholesterol efflux and LCAT activity of nascent HDL.** *A*, cholesterol efflux activity of human plasma isolated HDL (*pHDL*), reconstituted nascent HDL containing purified human apoA-I from healthy donors (*rHDL*), and reconstituted nascent HDL containing recombinant human apoA-I purified from *E. coli* (*rrHDL*) were measured by incubating different HDLs with subconfluent J774A.1 murine macrophage cells loaded with [^{3}H]cholesterol. The cholesterol efflux was calculated by radioactivity in the medium divided by the total radioactivity (medium radioactivity plus cell radioactivity) as described under "Experimental Procedures." Note that all three different HDLs have similar cholesterol efflux activity. *B*, rrHDL activates LCAT similarly as rHDL. LCAT activity was measured as described under "Experimental Procedures." Note that rrHDL retains at least 85% of LCAT activation capacity compared with rHDL. *C*, dissociation constants of nascent HDL·LCAT complex determined by surface plasmon resonance spectroscopy. The K_d value of binding between the indicated HDL and recombinant human LCAT was determined as described under "Experimental Procedures." Note that rHDL and rrHDL demonstrate a similar affinity with LCAT. *D*, Hanes and Woolf (*S/V versus S*) plot. The kinetic parameters of LCAT activity on rrHDL are similar to what is reported in the literature (K_m, V_{max}, and k_{cat}) (77, 78). All experimental results represent mean ± S.D. of three independent experiments.

vent matches the average scattering length density of the lipid phase masking it at low angle. However, the initial low resolution structure of apoA-I obtained by analysis of the scattering curve at 12% D_2O was inconclusive (*i.e.* not useful for determining the overall shape of the protein), presumably because of the weak signal intensity from protein at this D_2O level and the superposition of the residual signals produced by lipid polar head group scattering at higher angles. To overcome the issue of superimposed signals, we generated recombinant deuterated apoA-I (by growing *E. coli* in D_2O with deuterated nutrients) for use in forming reconstituted nascent HDL. Because of the difference in the scattering length of hydrogen and deuterium (58), the deuterated apoA-I gives a much stronger signal in 12% D_2O solvent.

Physical and biological properties of nascent HDL formed using recombinant deuterated apoA-I again demonstrated a biologically active particle with the compositional and functional characteristics indistinguishable with reconstituted HDL particle preparations generated with apoA-I isolated from human plasma. The experimental scattering intensity data from deuterated apoA-I within nascent HDL in 12% D_2O (Fig. 4*A*) allowed direct visualization of the overall time-averaged conformation of apoA-I following the simulated annealing method for *ab initio* structure determination (45). Unexpectedly, this low resolution SANS shape turned out to have an open helical conformation (Fig. 4, *B* and *C*). Other measured parameters for the apoA-I component of HDL include a radius of gyration (R_g) of 51 Å, and the longest dimension (D_{max}) of the protein to be ~170 Å (Table 1).

SANS Analyses of Nascent HDL Readily Discriminate among HDL Models—Because hydrogen and deuterium have markedly different neutron scattering properties, we have used a modified program to predict the scattering curve for all-atom structures of nonspherical macromolecular targets (supplemental material) (54). Visual inspection of the calculated theoretical scattering curves of more prominent models of HDL, the belt (18, 19) and solar flares models (23), reveals significant deviations between the predicted and experimental SANS curves (Fig. 4*A*). Both the belt and solar flares models deviate from the experimental SANS data at lower scattering angles and generate oscillatory scattering curves with minima and maxima characteristic of a ring shape at larger scattering angles. In additional investigations, we evaluated the scattering behavior of alternative proposed shapes for apoA-I in nascent HDL, such as saddles of differing curvature (supplemental Fig. S3) (63) or protein shapes with hairpin loop conformation for what historically is termed helix 5 (supplemental Fig. S4) (21). Again, because of the closed symmetrical shape of apoA-I in these models, the scattering curve demonstrates marked variation from that observed experimentally, including oscillatory behavior

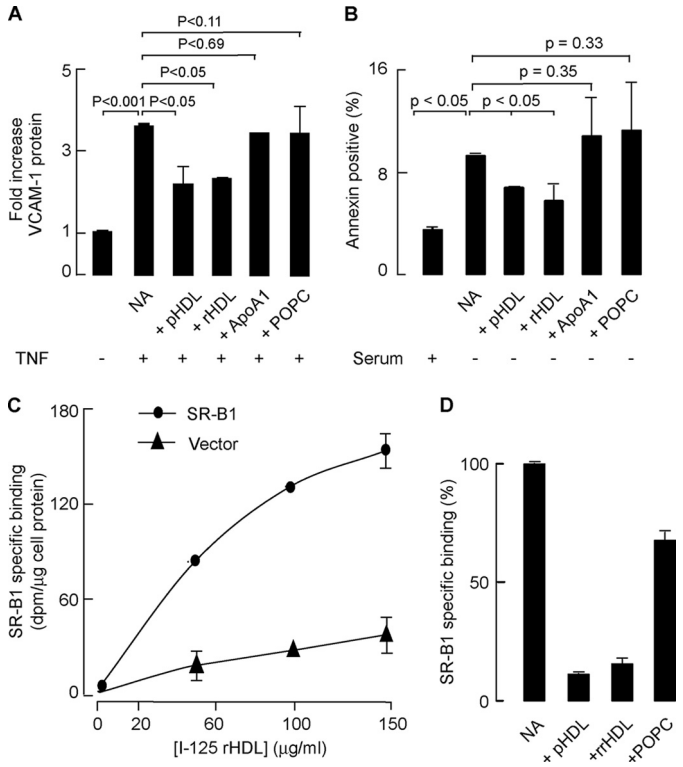

FIGURE 3. **Additional biological activities of nascent HDL.** *A*, demonstration of anti-inflammatory activity of HDL preparations. The capacity of the indicated HDL preparations (or their individual components) to inhibit tumor necrosis factor-α-induced enhanced VCAM-1 protein expression in HUVEC cells was determined by cell-based ELISA as described under "Experimental Procedures." Note that both human HDL (*pHDL*) and reconstituted nascent HDL containing purified human apoA-I from healthy donors (*rHDL*) prevent VCAM-1 expression following tumor necrosis factor stimulation. *B*, demonstration of anti-apoptotic properties of HDL preparations. Apoptosis was induced in HUVEC by 6 h of serum starvation. Cells were incubated simultaneously with pHDL, rHDL, apoA-I, or POPC, and the capacity of the indicated HDL particle (or its components) to inhibit apoptosis was determined as described under "Experimental Procedures." Note that both the pHDL and rHDL similarly protect HUVEC from apoptosis. *C*, specific binding of HDL preparations to HDL receptor SR-BI. Binding was determined in SR-BI- and vector-transfected 293-T cells by addition of iodinated rHDL. Specific binding was calculated as described under "Experimental Procedures." *D*, competition binding assay of SR-BI. The capacity of the indicated HDL preparation to act as a competitor and block SR-BI-specific binding of HDL isolated from plasma was determined as described under "Experimental Procedures." HDL isolated from plasma was iodinated and used as ligand, and competition binding studies were performed with 30-fold excess nonlabeled plasma HDL, the indicated reconstituted HDL, including reconstituted HDL made from recombinant human apoA-I (*rrHDL*), and small unilamellar vesicles (*SUV*) made of POPC. SR-BI-specific binding of iodinated human HDL is considered 100%. *NA*, no addition.

similar to the belt and solar flares models. SANS analyses indicate that closed symmetrical protein structures such as proposed in the belt, solar flares, and other ring models do not accurately represent the shape of apoA-I within recombinant nascent HDL, but rather they reveal that an open helical conformation for apoA-I is fully supported by the SANS data.

Double Superhelix Model for ApoA-I within Nascent HDL—Although SANS is a powerful approach for defining overall shape at low resolution, it is insensitive to local conformation at the level of amino acids and small peptides. In contrast, HD-MS/MS provides structural and dynamic information about the local environment of the amide protons throughout the polypeptide backbone at the amino acid or short peptide level of resolution but is relatively insensitive to global particle shape. Hydrogen/deuterium exchange data can provide structural constraints for protein architecture and dynamics in solution, and it is frequently used in NMR-based structural studies for the study of the local environment of amino acid residues in various protein secondary structures (helix, pleated sheets, etc.). H/D exchange of amide backbone hydrogen atoms is influenced by both solvent accessibility and protein dynamics, which reflect specific local interactions such as participation in hydrogen bonds within α-helices, hydrophobic contacts, etc. (25).

We therefore sought to integrate for the first time structural information from both contrast variation SANS and HD-MS/MS to extend the low resolution SANS structures for HDL through development of computational models that accommodate both the overall global shape dictated by SANS and the constraints imposed by measured hydrogen/deuterium exchange data for apoA-I within nascent HDL. Thus, a new model of apoA-I was built utilizing the low resolution SANS structure of HDL protein (Fig. 4*B*, *left*, and supplemental Fig. S5) as scaffold for the construction of an initial computational model of apoA-I. The starting model was energy-minimized and refined through iterative calculations of SANS intensity and H/D exchange incorporation factors (supplemental Figs. S5 and S6 and Table S5). Subsequently, additional geometrical constraints (experimentally determined cross-linking/mass spectrometry, fluorescence resonance energy transfer, and electron spin resonance coupling distance constraints (20, 21, 48)) were used to further refine the overall shape of the protein within the computational model. Clashes between atoms produced during modeling were removed by performing energy minimization at each step. Next, a model of the lipid phase of HDL was constructed based upon the experimental SANS structure of the lipid core (supplemental Fig. S7) and the model of apoA-I within HDL. The computational model developed for the solution structure for nascent HDL (called the double superhelix model because of the superhelical structure of the anti-parallel α-helical apoA-I chains) was thus obtained by combining all experimental data (SANS, HD-MS/MS, cross-linking/mass spectrometry, fluorescence resonance energy transfer, and electron spin resonance coupling) with integrative computational modeling tools (see supplemental material).

The predicted structure of apoA-I within the double superhelix model of nascent HDL is shown in Fig. 4*B* (*right*). Fig. 4*A* shows the calculated scattering intensity of the double superhelix model (*blue line*), which fits very well the experimental scattering intensity curve. As in the previous belt and solar flares models, the protein in the double superhelix model has the two apoA-I chains in predominantly α-helix secondary structure and in anti-parallel orientation (Fig. 4*B*, *right*). The open helical conformation of the two apoA-I molecules is readily visualized in Fig. 4*C*, which provides a different vantage point of the low resolution SANS shape (*left*), the high resolution protein in the double superhelix model (*middle*), and their overlap (*right*). The relatively hydrophobic surface of apoA-I is oriented inward, indicating the groove formed within the helical protein spiral abuts a central lipid core (Fig. 4*D*). In contrast,

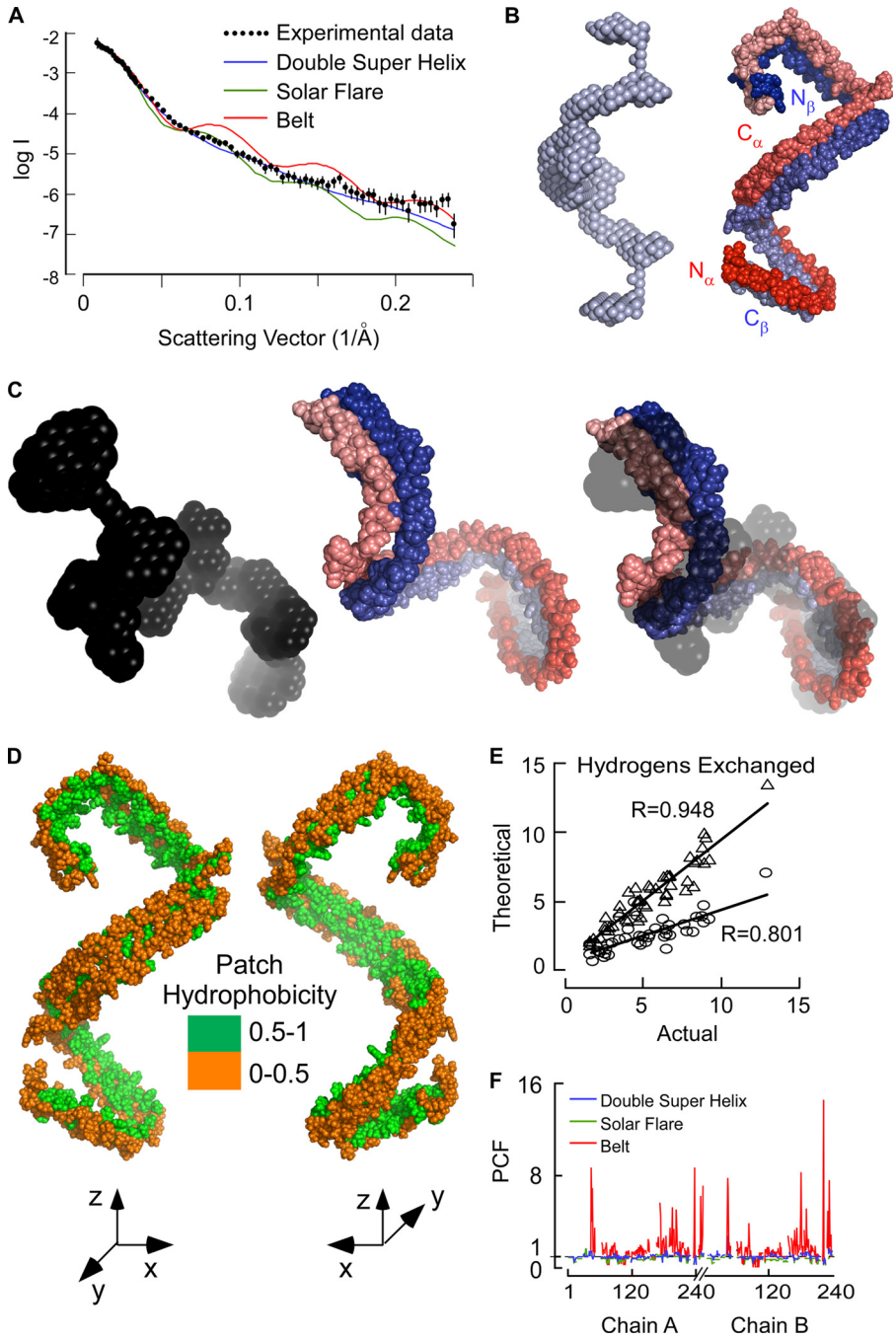

FIGURE 4. **Superhelical structure of apoA-I within nascent HDL revealed by SANS and HD-MS/MS.** *A,* comparison of experimental SANS intensity from deuterated apoA-I-nascent HDL in 12% D_2O buffer (*black dotted line*) with calculated intensity of the double superhelix model (*blue line*), solar flares model (*green line*), and belt model (*red line*). *B,* SANS low resolution structure of apoA-I reconstructed from the experimentally obtained scattering curve of nascent HDL (*left*) and the all-atom double superhelix model of apoA-I within nascent HDL (*right*). *C,* 12% D_2O SANS shape (*black*), apoA-I in the double superhelix model (*red-blue*), and their overlap from a viewing angle that emphasizes the helical conformation of the protein; N termini are colored in *dark red/blue* and C termini in *light red/blue*. *D,* map of "patch" hydrophobicity of apoA-I within nascent HDL in the double superhelix model. Like the hydrophobic index, the patch hydrophobicity is in the range [0,1] and is determined for each amino acid residue by averaging the hydrophobic indices of neighboring residues (*e.g.* within 15 Å) located on the same side of protein, *i.e.* either inside (facing lipid) or outside (facing solvent) (79). *E,* correlation (*R*) between the experimentally measured deuterium incorporation factors (D_0) for apoA-I peptic peptides from nascent HDL *versus* the predicted (calculated) D_0 values for both the belt (*open circle*) and double superhelix (*open triangle*) models of nascent HDL. *F,* "goodness of fit" of the double superhelix, solar flares, and the belt models at the individual residue level. The probability correction factor (*PCF*) plotted on the *y* axis represents the multiplier needed to adjust the exchange probability of individual residues within the model to match that determined by hydrogen/deuterium exchange mass spectrometry studies. The *dashed line* at unity represents the probability correction factor of a given amino acid within the model that possesses a conformation with the same H/D exchange as observed by experimental measurement.

the majority of hydrophilic amino acids are oriented toward the outer solvent-exposed surface (Fig. 4*D*). It is worth noting that to accommodate the HD-MS/MS data the N termini of apoA-I are predicted to have predominantly α-helix secondary structure as suggested previously (64).

More quantitative analyses of the goodness of fit of experimental SANS and HD-MS/MS data and the double superhelix model are shown in both Table 1, and Fig. 4, *E* and *F*. Calculated χ^2 statistics that quantify differences between the experimentally determined and theoretical scattering intensities show superior fit for the double superhelix model compared with belt and solar flares models. Similarly, a close correlation is observed between experimental HD-MS/MS data and that predicted for the double superhelix model at both peptide (Fig. 4*E*) and amino acid levels of resolution (Fig. 4*F*). The predicted conformation of apoA-I in the double superhelix model demonstrates substantially improved fit with experimental HD-MS/MS data, compared with that predicted for apoA-I in the belt model, and a similar fit of experimental HD-MS/MS data in the solar flares model (Fig. 4*F* and Table 1).

Lipid Core of Nascent HDL Is Ellipsoidal—To visualize directly the structure of the lipid core of nascent HDL, we performed SANS at 42% D_2O contrast variation (Fig. 5*A*, *black dotted line*). The HDL particles studied this time were generated with nondeuterated human apoA-I isolated from plasma. At 42% D_2O, the solvent closely matches the scattering length density of the nondeuterated protein (match point 42%) and to a lesser extent the lipid polar head groups (match point 30%), thus leaving mainly the acyl chains (match point ~3%) of the lipid visible (58). The experimental radius of gyration obtained for the lipid core is 39.7 Å, which is about 10 Å smaller than the radius of gyration of the protein (51.3 Å). These results confirm that the protein component of HDL is located predomi-

TABLE 1

Goodness of fit of HDL models with experimental SANS, EM, and HD-MS/MS data

Radius of gyration, global dimensions, and goodness of fit of HDL models with experimental SANS, EM, and HD-MS/MS data are shown. Physical parameters, including radius of gyration (R_g) and overall dimension of the double superhelix model of nascent HDL, are more consistent with the values measured both by SANS and small angle x-ray scattering (SAXS) compared with the existing models of nascent HDL. Calculated χ^2 statistics that quantify differences between the experimentally determined and theoretical scattering intensities show superior fit for the double superhelix model compared with belt and solar flares models. More quantitative analysis of goodness of fit of HDL models with HD-MS/MS data, including root mean square deviation (r.m.s.d.), probability correction factor (PCF), and correlation coefficient, suggest that the double superhelix model fits better with the experimental data than the belt and solar flares models. l is length, w is width, and h is height.

Models	Radius of gyration (Å)			Dimensions (Å), l × w × h	χ^2 [a]		Correlation coefficient[b]	r.m.s.d.[c]		
	HDL	Protein	Lipid		Protein	Lipid		Peptide	PCF[d](α)	PCF(β)
Experimental										
SAXS	52.0			167						
SANS		51.3	39.7	171 × 74 × 69						
EM				160 × 60						
Double superhelix		52.1	38.4	171 × 73 × 67	1.1	145	0.946	0.82	0.21	0.24
Solar flares		53.4	33.7	140 × 115 × 50	6.9	497	0.915	1.65	0.30	0.29
Belt		47.2	30.2	98 × 98 × 45	12.7	2,255	0.794	2.39	1.50	1.72

[a] χ^2 stands for the standard deviations between the experimental scattering data and calculated scattering data of nascent HDL models obtained from our modified SASSIM Program54.

[b] Correlation coefficient was correlation between theoretical hydrogen/deuterium exchange probabilities of peptic peptides in the model and the actual experimentally measured deuterium incorporation within apoA-I peptic peptides.

[c] r.m.s.d. stands for root mean square deviation. It quantifies the difference between the experimental deuterium exchange data and the calculated ones.

[d] PCF stands for probability correction factor, which represents the multiplier needed to adjust theoretical deuterium incorporation of individual residues based upon the HDL models to match that which was actually experimentally determined.

nantly toward the outside of the particle, although the phospholipid acyl chains occupy a more central location within the HDL. The low resolution structure of the lipid core was initially reconstructed from the experimental SANS data obtained from nascent HDL solvated with 42% D_2O (Fig. 5*B* and supplemental Fig. S7). The overall structure of the HDL particle lipid core visualized is clearly prolate ellipsoid. Next, we built a hypothetical initial all-atom model for the lipid of nascent HDL. As proposed in earlier HDL models, the hydrophobic portion of the lipids interacts with the hydrophobic surface of the protein, and the lipid polar head groups are oriented toward the aqueous phase. We thus used as scaffold for the initial model of the lipid both the helical groove partially bounded by the hydrophobic surface of the anti-parallel apoA-I chains and the overall ellipsoidal structure of the lipid core visualized by SANS (supplemental Fig. S5 and S7 and Table S5). Hydrophobic acyl chains of phospholipids were oriented toward the hydrophobic protein surface (*e.g.* Fig. 4*D*) of the apoA-I helix. The initial model was refined through iterative energy minimizations and evaluations of the goodness of fit of SANS intensity for both protein and lipid core shapes and amide proton solvent accessibility throughout the entire polypeptide chain. In this manner, we optimized the HDL structure such that minimal differences between predicted *versus* experimental data (for both SANS and HD-MS/MS) were achieved. Subsequently reported cross-linking/mass spectrometry, fluorescence resonance energy transfer, and electron spin resonance coupling distance constraints (20, 21, 48) were used as additional geometrical constraints for the overall shape of the protein within HDL, and then a final energy minimization of the intact solvated particle was performed (see supplemental Fig. S5, S6, and S7 and Table S5). Molecular dynamics simulation was also performed (supplemental Fig. S9) on the final computational model, the double superhelix model of nascent HDL, revealing a thermodynamically stable particle that retained overall helical conformation of apoA-I and preserved both the lipid organization and solvent-exposed protruding apoA-I loops in the region previously identified as the LCAT-binding site in HDL (also known as the solar flares (23)).

The structural model proposed for the lipid within the double superhelix model of nascent HDL is shown in Fig. 5*C*. The overall lipid mesophase is predicted to be predominantly micellar, while adopting a pseudolamellar arrangement in the vicinity of the protein. It should be noted that if one assumes that the packing arrangement of the lipid is essentially dictated by the shape of the superhelical protein component of nascent HDL, orienting the acyl chains toward the hydrophobic amphipathic protein surface, an ellipsoidal lipid micelle is generated with overall shape compatible with the low resolution structure visualized for the lipid core of HDL (Fig. 5, *B* and *C*). Comparison of the overall lipid shapes within various HDL models demonstrates the structure posited for the double superhelix model is more closely aligned with the experimental SANS scattering data collected in 42% D_2O (Fig. 5*A*). Furthermore, the calculated scattering intensity of lamellar mesophase (bilayer) lipids for both belt and solar flares models are more skewed away from the experimental SANS curve at lower scattering angles, suggesting poorer fit with the experimental data (Fig. 5*A*). This is confirmed by quantitative analysis of the goodness of fit of the predicted scattering curves derived from the shape of the lipid core of the double superhelix model *versus* both solar flares and belt models, where significantly greater deviation from the experimental SANS scattering data is observed with both the solar flares and belt models, as indicated by the substantially larger χ^2 statistics (Table 1).

Global Dimensions of the Double Superhelix Model of Nascent HDL—The overall dimensions of the experimentally determined low resolution (SANS) structures for nascent HDL and the double superhelix model are illustrated in Fig. 6, *A–D*. Of note, the particle model is a prolate ellipsoid with global proportions in close agreement with that observed by both SANS and EM (Fig. 6, *A–D*, and Table 1). The anti-parallel nature of the two apoA-I α-helices are predicted to be stabilized by multiple inter-chain salt bridges (Fig. 6*C* and supplemental Table S7), providing structural support for the protein to serve as a superhelical scaffolding upon which HDL lipids are transported. Individual particles in EM images correspond to projections of an ellipsoid of 55–65 Å in diameter and ~160 Å in

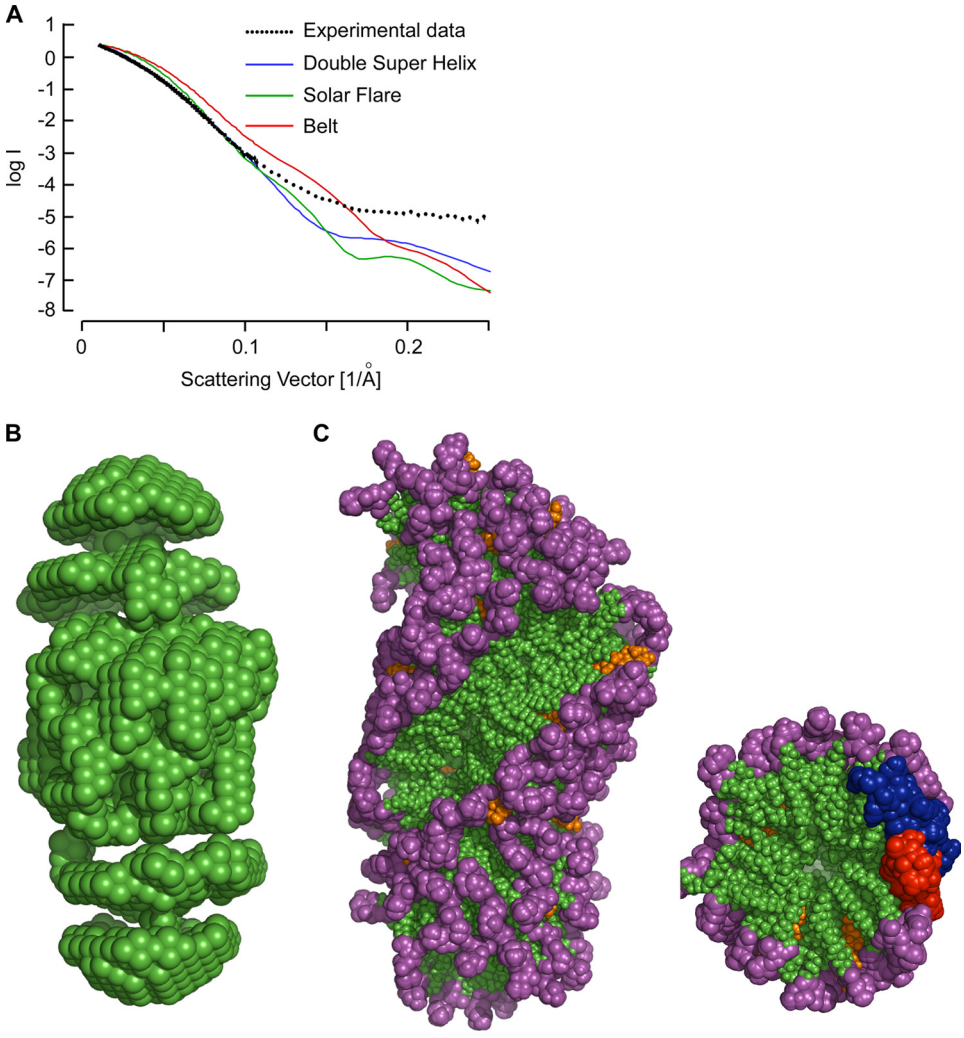

FIGURE 5. **Prolate ellipsoid structure of the lipid core within nascent HDL revealed by SANS.** *A,* comparison of experimental SANS intensity (*black dotted line with error bars*) at 42% D_2O with the scattering intensity of the double superhelix (*blue line*), solar flares (*green line*), and belt models (*red line*). *B,* low resolution SANS structure of lipid core within nascent HDL reconstructed from the scattering intensity of nascent HDL in 42% D_2O solution. *C,* all-atom model of lipids in the double superhelix model of nascent HDL illustrating both pseudo-lamellar and micellar organizational features. The phosphatidylcholine headgroups are colored *purple*; the phospholipid acyl chains are *green*, and cholesterol is *orange* (*left*). The prolate ellipsoid view (*left*) shows the pseudo-lamellar arrangement of lipids where the helical protein sits (protein not shown; note the end-on-end orientation of the acyl chains within the grove where the apoA-I has been removed). The cross-sectional view (*right*) illustrates the micellar-like packing of lipids. The two apoA-I chains are shown as *red* and *blue*.

length under different orientations. The internal structure of the particles was not clearly discernable on EM, even after an enhancement of the signal to noise ratio by classification, alignment, and averaging. Nonetheless, some class averages display striations reminiscent of projections of the proposed double superhelix model for HDL. Independent studies employing small angle x-ray scattering yielded similar particle dimensions (Table 1 and supplemental Fig. S8). The α-helical content of apoA-I within the double superhelix model as estimated by PyMOL is 68%, similar to that observed by circular dichroism measurements on the recombinant HDL particles (67%), and is in close agreement with values reported previously (65). Finally, better than the earlier prominent HDL models reported in the literature, all sequence-confirmed intra-chain and most inter-chain distance constraints identified for apoA-I based upon mass spectrometry analyses in cross-linking studies (20, 48), fluorescence resonance energy transfer (21), or electron spin resonance studies (21) are accommodated by the superhelical conformation of apoA-I in the double superhelix model (Table 2 and supplemental Fig. S4 and Table S6). An inter-chain cross-link previously reported (20, 48) that would be structurally forbidden within a single HDL particle (Lys^{208}–Lys^{208}) could be readily accommodated by a cross-link formed between a pair of particles such as with rouleaux formation.

DISCUSSION

Biological Implications and Context with Prior Studies—The model of nascent HDL presented here is a dramatic and surprising departure from the entrenched view. The open helical low resolution shape of apoA-I visualized by SANS should allow for a highly versatile particle that can accommodate alterations in shape and lipid composition during particle maturation and remodeling, properties that undoubtedly facilitate the ability of the particle to support its transport function. The superhelical conformation of apoA-I helps to envision a path of HDL particle genesis from poorly lipidated apoA-I through association of phospholipid and sterol with a gradually unfolding protein. Furthermore, the free energy barrier for assembling the lipid phase posited in the double superhelix model should be less than that required for constructing a circumferentially enshrined bilayer during HDL particle genesis such as required by discoidal (*i.e.* belt and solar flares) models. Moreover, selective uptake, exchange, or modification of lipids within HDL during interaction with both its cell-based receptors or plasma enzymes will not generate an immediate asymmetric distribution of lipids within the particle (*i.e.* a "heads" *versus* "tails" to the disk), a problem intrinsic to all discoidal/bilayer-containing models of HDL that to date has not been adequately addressed. In contrast, lipids in the double superhelix model are free to diffuse throughout the entire particle.

Nearly 3 decades ago, Atkinson *et al.* (66) reported the first structural studies of HDL employing SANS with contrast variation. Although the detailed topography of protein and lipid components remained undefined, the authors concluded that the protein of HDL is located circumferentially relative to lipid

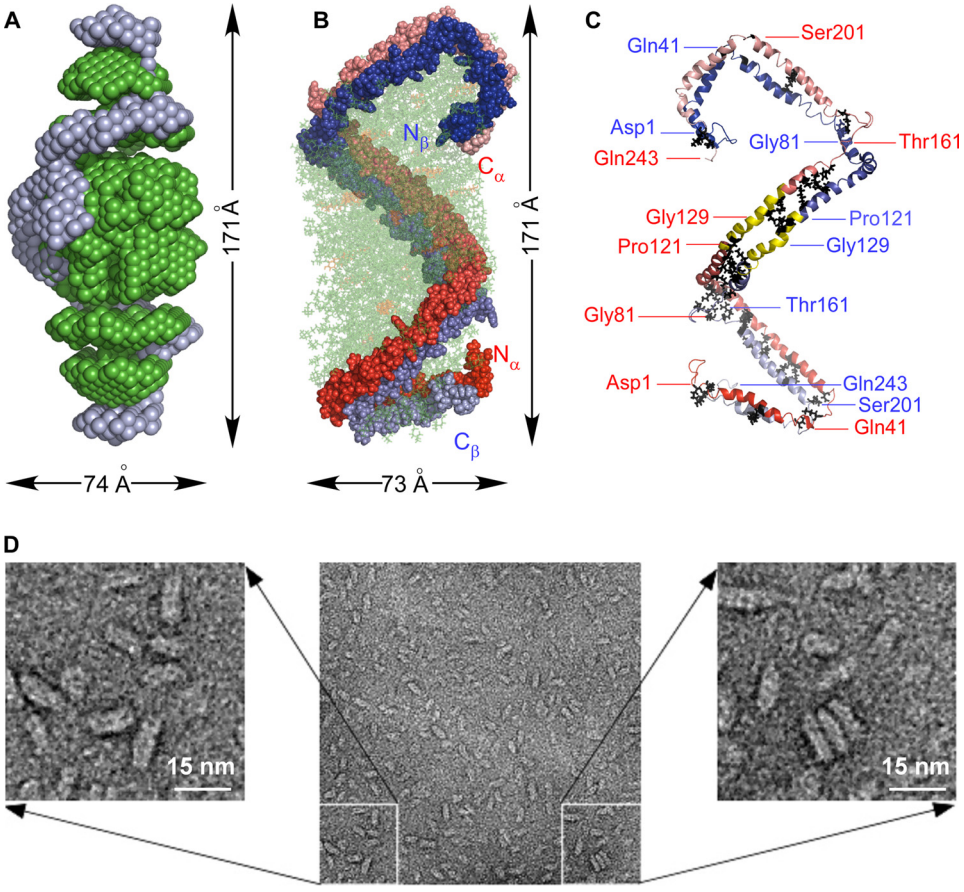

FIGURE 6. **Geometrical dimensions and electron microscopy imaging of nascent HDL.** *A,* overlay of the SANS low resolution structures of apoA-I (*light blue*) and lipid core (*green*) within nascent HDL. The lipid core structure shows clear invaginations that are approximately filled by protein. *B,* overlay of apoA-I and lipid all-atom double superhelix model of nascent HDL. The superhelical shape of the protein is emphasized by the *semi-transparent* representation of the lipid core, in which phospholipid is depicted in *green* and cholesterol in *orange*. *C,* illustration of the anti-parallel amino acid arrangement proposed in the double superhelix model of apoA-I in nascent HDL. The two apoA-I molecules are aligned in a head to tail anti-parallel arrangement using a helix 5/helix 5 registry (*yellow*). The N termini are colored with *dark red/blue*, and the C termini are colored with *light red/blue*. Twenty eight inter-chain salt bridges that stabilize the anti-parallel double superhelical conformation of apoA-I are also illustrated as *sticks*. *D,* characteristic negative stain electron microscopic image of nascent HDL, along with two expanded views of the indicated *insets*. The *scale bar* corresponds to 15 nm.

containing apolipoprotein E and an ellipsoidal shaped lipid core with posited phospholipid packing similar to a micelle, which they termed the "twisted bilayer" model.

Prior computational modeling for nascent HDL has suggested a discoidal particle composed of a double belt conformation of apoA-I encircling a lipid bilayer (18). This was based upon studies of particles with alternative composition (*e.g.* 80:1, mol/mol, PC:apoA-I) and with an N-terminal (Δ43) truncated apoA-I, the initial form of lipid-free apoA-I crystallized (70). The HDL particle composition selected for this study, the methods for particle generation, and the detailed functional characterizations performed demonstrate a biologically active particle similar in composition to nascent HDL (96 Å form) generated by macrophages (31). Moreover, the reconstituted HDL preparations examined have similar composition to those used in many recent HDL-based human therapeutic intervention trials (9, 28, 30, 71, 72). Although the present study focuses solely on a single reconstituted HDL form similar in composition and biological activities to nascent HDL, we cannot exclude the possibility that HDL particles composed of different protein/lipid compositions and alternative apolipoprotein polypeptide chain lengths may assume different global architecture and lipid organization. The lipid structural studies performed do not directly visualize the detailed packing arrangement of the lipid of HDL and thus do not exclude the possibility of an alternative organization.

within the particle and suggested a bilayer disk (oblate ellipsoid) model for HDL. Additional studies on reconstituted HDL performed by SAXS without contrast variation and molecular dynamics simulations (67, 68) either lent support to the idea of HDL being discoidal or did not define a low resolution model of nascent HDL with contrast variation. In preliminary SANS studies, we similarly could not define the low resolution shape of apoA-I within HDL because of both a weak protein signal and the overlap between the scattering signal from protein and phospholipid at higher angles. The use of deuterated apoA-I for nascent HDL generation proved key in permitting direct visualization of the open helical conformation of the protein within the HDL particle. Moreover, the helical architecture of the protein within HDL suggests a predominantly micellar and pseudo-lamellar organization of the lipids within the prolate ellipsoidal shape visualized by SANS for the lipid core of nascent HDL. It is of interest that Weisgraber and co-workers (69) used small angle x-ray scattering to explore the structure of apolipoprotein E-dipalmitoyl phosphatidylcholine particles in solution and observed a "quasi-spheroidal" particle with hairpin-

The computational model of nascent HDL (the double superhelix model) was obtained by combining the low resolution structures obtained by SANS with contrast variation and selective deuteration of apoA-I and data from multiple experimental studies of HDL using novel integrative computational methods (*e.g.* HD-MS/MS, cross-linking/mass spectrometry, fluorescence resonance energy transfer, and electron spin resonance coupling). Interestingly, although no crystal structures of lipid-free apoA-I were used (other than the incorporation of an anti-parallel orientation of apoA-I chains as originally suggested by the lipid free Δ43-N-terminal truncated apoA-I mutant (70)), it is remarkable to note that the conformation of apoA-I in the double superhelix model contains several turns found in the recently reported crystal structure of lipid-free full-length apoA-I (Protein Data Bank code 2A01) (73). As Fig. 7*A* shows,

TABLE 2

Goodness of fit of HDL models with experimental SANS, EM, and HD-MS/MS data

Amino acid distance constraints between α and β chains of apoA-I within nascent HDL obtained from fluorescence resonance energy transfer (FRET), HPLC tandem mass spectrometry (MS/MS), and electron spin resonance coupling (ESR) are shown.

Residues	Double helix model	Methods
	Å	
Trp^{50}–Leu^{230}	22.8[a]	FRET (22.7 Å)[b]
Trp^{72}–Ala^{210}	30.2	FRET (23.5 Å)[a]
Leu^{90}–Ala^{190}	26.2	FRET (24.0 Å)[a]
Trp^{108}–Leu^{170}	26.6	FRET (28.8 Å)[a]
Gln^{132}–Gln^{132}	17.3[c]	FRET (30–35 Å)[a]
Lys^{40}–Lys^{239}	30.1[d]	MS/MS (12 Å)[e,f,g]
Lys^{118}–Lys^{140}	10.7	MS/MS (12 Å)[e,f,g]
Lys^{12}–Lys^{182}	16.1	MS/MS (12 Å)[e,g]
Lys^{59}–Lys^{208}	15.6	MS/MS (12 Å)[f]
Lys^{77}–Lys^{195}	18.1	MS/MS (12 Å)[f]
Lys^{133}–Lys^{140}	6.4	MS/MS (7.7 Å)[g]
Lys^{208}–Lys^{208} [h]	160.1	MS/MS (12 Å)[f]
Lys^{88}–Lys^{118} [h]	69.1	MS/MS (12 Å)[f]
Lys^{96}–Lys^{118} [h]	64.2	MS/MS (12 Å)[f]
Lys^{133}–Lys^{133} [i]	6.2	ESR (<15 Å)[a]
Glu^{146}–Glu^{146} [i]	43.8	ESR (<15 Å)[a]
Leu^{134}–Leu^{134} [i]	10.9	ESR (17–19 Å)[a]

[a] The calculated distances between two residues in the double superhelix model of nascent HDL are from the far end of the side chain of Trp to the far end of N-acetylaminoethyl-1-aminonaphthalene sulfonate acceptor assuming free rotation of the side chain of amino acids.
[b] Data are from Martin *et al.* (21).
[c] Data are from Li *et al.* (80).
[d] The calculated distances in the double superhelix model of nascent HDL are between ϵ-amine groups of two lysines assuming free rotation of the side chain of lysines.
[e] Data are from Bhat *et al.* (20).
[f] Data are from Silva *et al.* (48).
[g] Data are from Bhat *et al.* (81).
[h] Data are not compatible with 5/5 registry.
[i] The calculated distances between two residues in the double superhelix model of nascent HDL are from the oxygen atom of methane thiosulfonate nitroxide spin label on one residue to the oxygen atom of methane thiosulfonate nitroxide spin label of the other residue.

there are five turning loops in the reported crystal structure of lipid-free apoA-I (Protein Data Bank 2A01) that start with leucine and most of them end with leucine (Leu^{38}–Leu^{47}, Leu^{82}–Ala^{95}, Leu^{137}–Leu^{144}, Leu^{189}–Ala^{196}, and Leu^{214}–Leu^{218}). Three of these turns (Leu^{38}–Leu^{47}, Leu^{82}–Ala^{95}, and Leu^{214}–Leu^{218}) are also present as turns in the double superhelix model of apoA-I (Fig. 7*B*). Interestingly, a bend is also observed in both chains of apoA-I of the double superhelix model at the remaining two turns of lipid-free apoA-I (Fig. 7*B*). Moreover, one of these turns (Fig. 7*B, turn 3*) partially forms following molecular dynamics simulation of the double superhelix model (supplemental Fig. S9) and corresponds to a region on apoA-I suggested by Oda and co-workers (21) to adopt a hairpin loop structure. These studies relied upon multiple site-specific mutated forms of apoA-I combined with derivatization with detector molecules (*e.g.* spin adducts or bulky aromatic species). Although one of the inter-chain distance constraints observed (*e.g.* position 133 on each chain) is readily satisfied in the double superhelix model (Table 2), another one (position 146 on each chain) is not (Table 2). By changing the registry of the two apoA-I chains, this inter-chain distance constraint can be accommodated; however, this also results in a structure that no longer satisfies some of the reported cross-links (supplemental Fig. S4). It should also be noted that introduction of a loop within the helix 5 region of apoA-I of the double superhelix model causes the following to occur: (i) reduces the agreement of the predicted SANS scattering curve with the experimental SANS data; (ii) deteriorates the goodness of fit between experimental and theoretical HD-MS/MS deuterium incorporation factors for this region; and (iii) renders some of the reported cross-links forbidden regardless of whether the loop is introduced into the double superhelix or belt models of apoA-I (supplemental Fig. S4). In contrast to studies with SANS and HD-MS/MS, which are nonperturbing, studies that employ mutations of apoA-I, while informative, need to be interpreted within the context of recognizing that structural and functional alterations to the particle may be introduced. For example, HDL particles generated with recombinant mutant apoA-I that lack all four of the endogenous tryptophan residues, the mutant form of apoA-I often used as a backbone for additional site-specific mutants studied by fluorescence resonance energy transfer and electron spin resonance, can have markedly impaired cholesterol efflux function depending upon the amino acid used to replace the tryptophan (74). Our present studies do not rule out the possible formation of transient loop structures anywhere throughout the apoA-I polypeptide because the overall shape of the proposed double superhelix model arises from the overall time-averaged conformation of apoA-I within the ensemble of various nascent HDL conformations in solution visualized by SANS. Indeed, the double superhelix model readily accommodates a highly dynamic conformation of apoA-I while retaining lipid binding properties within the particle. Although the precise location of small structural elements along the apoA-I chain of nascent HDL may still be debated, the studies reported here suggest that the overall time-averaged global architecture of apoA-I within nascent HDL (at least for the studied lipid/protein composition) is an open spiral (Fig. 7, *C* and *D*).

Another remarkable feature of the double superhelix model of nascent HDL is that numerous previously reported structural constraints (inter-chain distances based upon cross-linking/mass spectrometry, fluorescence resonance energy transfer, and electron spin resonance studies) used to argue in favor of prior models can be readily accommodated within the observed open helical conformation of apoA-I (Table 2 and supplemental Table S6). Moreover, some regional structural features proposed in prior studies that were not easily accommodated by the closed belt structures can be more readily accommodated within the open and dynamic apoA-I helical conformation. For example, Thomas and co-workers (20) reported that the N terminus of apoA-I folds back upon the apoA-I chain allowing for detection of a cross-link between inter-chain residues Lys^{12} and Lys^{182}. Another intra-chain cross-link between Lys^{94} and the apoA-I chain N terminus was similarly reported by Davidson and co-workers (48). The double superhelix model accommodates the cross-link between Lys^{12} and Lys^{182} (Table 2). Furthermore, small changes in the conformation of the N-terminal region of apoA-I readily bring the N terminus and Lys^{94} within permissible distance for cross-linking (supplemental Fig. S10).

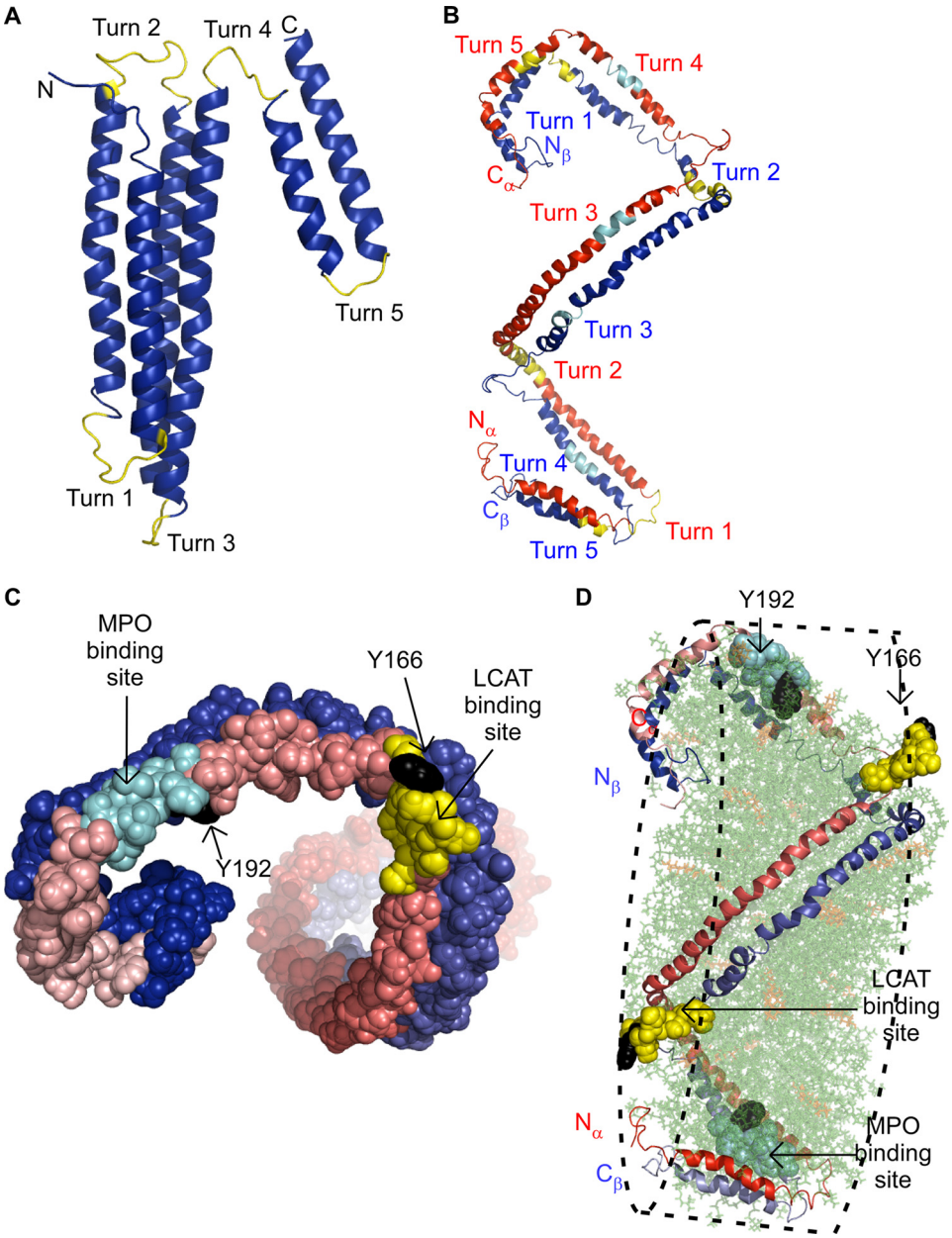

FIGURE 7. **Double superhelix model of nascent HDL.** *A* and *B*, illustration that apoA-I within nascent HDL retains structural features of full-length lipid-free apoA-I. *A*, crystal structure of lipid-free apoA-I (73) with residues in the turning loops colored in *yellow*: Leu^{38}–Leu^{47} (*turn 1*); Leu^{82}–Ala^{95} (*turn 2*); Leu^{137}–Leu^{144} (*turn 3*); Leu^{189}–Ala^{196} (*turn 4*); and Leu^{214}–Leu^{218} (*turn 5*). *B*, turns in lipid-free apoA-I mapped onto the double superhelix model of apoA-I. Turns in lipid-free apoA-I that no longer correspond to turns within the double superhelix model are colored in *cyan*. Turns 1, 2, and 5 from lipid-free apoA-I are also present in the double superhelix model. *C*, locations of the LCAT interaction site (residues 159–170, *yellow*) and myeloperoxidase (*MPO*)-binding site (residues 190–203, *light blue*) in the double superhelix model of apoA-I. Two residues, Tyr^{166} and Tyr^{192}, which undergo site-specific oxidative modifications within human atherosclerotic lesions, are shown in *black*. *D*, all-atom double superhelix model of nascent HDL with known protein-protein interaction sites; POPC (*green*) and cholesterol (*orange*) are viewed in *semitransparent* mode. The *dashed line* shown represents the hypothetical overlay of a discoidal model of HDL, showing overall similar size.

A structural feature predicted in the double superhelix model is the presence of two highly dynamic and solvated apoA-I loops previously identified to support LCAT docking and activation within nascent HDL, also known as the so-called solar flares (23). Molecular simulation studies performed on the double superhelix model (supplemental Fig. S9) support the dynamic character and solvent accessibility of apoA-I in this region and show that the "solar flares" remain highly solvent-exposed over prolonged simulation time (>4 ns), with breaking and reformation of salt bridges. This contrasts with a recently reported molecular dynamics simulation that claims that the solar flares "collapse" in the solar flares model because disruption of one or more predicted salt bridge as visualized in a single time frame of a brief (1 ns) simulation (75). Because no His in their model were protonated, the model they used for simulation differs from that employed in our past and present studies, as well as in other computational studies (*e.g.* the belt model (18)). As illustrated in Fig. 8, the experimentally measured deuterium incorporation factors for residues within the peptide corresponding to the solar flare loop (*e.g.* Arg^{160B}–Arg^{177B}) show a high degree of deuterium incorporation (average $D_0^i = 0.8$). This is because the residues within this region of apoA-I are very dynamic (derived average per residue unfolding equilibrium constant, $K_u^i \sim 10^{-2}$), and their amide hydrogens exchange rapidly (derived average per residue exchange rate constant, $k_{xc}^i \sim 0.23\ s^{-1}$), regardless of whether they are involved in H-bonding or not (see supplemental Table S3). In contrast, the amide hydrogens of the residues in the adjacent α-helix from the anti-parallel apoA-I chain (Lys^{77A}–Lys^{106A}), by comparison, show reduced deuterium incorporation (average $D_0^i = 0.47$), are substantially less dynamic ($K_u \sim 10^{-3}$), and their amide hydrogens exchange an order of magnitude slower ($k_{xc} \sim 2.67 \times 10^{-2}\ s^{-1}$) (Fig. 8).

Lipoproteins participate in numerous biological functions, including sterol and lipid transport, organismal energy metabolism, and innate immunity. Despite their central role in multiple pathophysiologically relevant processes, as a class, intact lipidated lipoproteins have defied high resolution structural characterization because of their heterogeneous composition, dynamic/polymorphic nature, and large size. This lack of structural definition hinders fundamental understanding of pathobiological processes and potential development of therapeutic interventions. By uniting the complementary and nonperturbing approaches of SANS and HD-MS/MS in

A

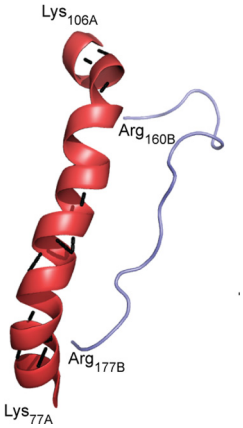

B

	D_0	K_u	K_{xc} (S^{-1})
α-Helix (Lys_{77A} - Lys_{106A})	0.47	2.04×10^{-3}	2.67×10^{-2}
Loop (Arg_{160B} - Arg_{177B})	0.80	2.72×10^{-2}	0.229
Fold difference	~ 2	~ 10	~ 10

FIGURE 8. **Solar flare region of nascent HDL in the double superhelix model.** *A,* predicted solution structure of peptide Leu^{159}–Arg^{177} (*blue*) in chain B of apoA-I in the double superhelix model of nascent HDL, and the adjacent α-helix from chain A (Lys^{77}–Lys^{106}, *red*). *B,* summary of average experimentally determined deuterium incorporation factors (D_0), average unfolding constants (K_u), and average exchange rate constants (k_{xc}) for the two peptides shown.

combination with computational and bioinformatic methods, we have applied a multidisciplinary and broadly applicable methodology for the structural study of solution phase macromolecular complexes resistant to traditional high resolution structural interrogation, such as lipoproteins. Application of this approach revealed a totally unexpected conformation of apoA-I in the nascent HDL particle, a double superhelix. Overall, the protein seems to play the role of a backbone giving mechanical strength to the HDL particle, while acting as an interface for both lipid binding/transport and specific interactions with plasma enzymes and cell receptors. The observed open helical shape of apoA-I, lipid arrangement, and overall ellipsoidal particle shape accounts for geometrical, biophysical, and biochemical data reported to date. It also has not escaped our attention that a helical shape for a protein scaffolding for a lipoprotein envisages a credible generalized pathway for lipoprotein biogenesis, maturation, and remodeling.

Acknowledgments—We thank Dimitri Svergun and Maxim Petouchov (EMBL Hamburg, DESY, Notkestrasse 85, 22603 Hamburg, Germany) for assistance in performance of SAXS analyses. We thank Dr. Segrest for providing the Protein Data Bank file of the belt model of HDL.

REFERENCES

1. Tall, A. R., Yvan-Charvet, L., Terasaka, N., Pagler, T., and Wang, N. (2008) *Cell Metab.* **7,** 365–375
2. Trigatti, B., Rigotti, A., and Krieger, M. (2000) *Curr. Opin. Lipidol.* **11,** 123–131
3. Barter, P. J., and Rye, K. A. (2006) *Curr. Opin. Lipidol.* **17,** 399–403
4. Rader, D. J. (2007) *Nat. Clin. Pract. Cardiovasc. Med.* **4,** 102–109
5. Assmann, G., and Gotto, A. M., Jr. (2004) *Circulation* **109,** III8–III14
6. Plump, A. S., Scott, C. J., and Breslow, J. L. (1994) *Proc. Natl. Acad. Sci. U.S.A.* **91,** 9607–9611
7. Chapman, M. J. (2006) *Pharmacol. Ther.* **111,** 893–908
8. Linsel-Nitschke, P., and Tall, A. R. (2005) *Nat. Rev. Drug Discov.* **4,** 193–205
9. Nissen, S. E., Tsunoda, T., Tuzcu, E. M., Schoenhagen, P., Cooper, C. J., Yasin, M., Eaton, G. M., Lauer, M. A., Sheldon, W. S., Grines, C. L., Halpern, S., Crowe, T., Blankenship, J. C., and Kerensky, R. (2003) *JAMA* **290,** 2292–2300
10. Shah, P. K., Nilsson, J., Kaul, S., Fishbein, M. C., Ageland, H., Hamsten, A., Johansson, J., Karpe, F., and Cercek, B. (1998) *Circulation* **97,** 780–785
11. Navab, M., Anantharamaiah, G. M., Reddy, S. T., Hama, S., Hough, G., Grijalva, V. R., Wagner, A. C., Frank, J. S., Datta, G., Garber, D., and Fogelman, A. M. (2004) *Circulation* **109,** 3215–3220
12. Tall, A. R. (2007) *N. Engl. J. Med.* **356,** 1364–1366
13. Nissen, S. E., Tardif, J. C., Nicholls, S. J., Revkin, J. H., Shear, C. L., Duggan, W. T., Ruzyllo, W., Bachinsky, W. B., Lasala, G. P., Lasala, G. P., and Tuzcu, E. M. (2007) *N. Engl. J. Med.* **356,** 1304–1316
14. Barter, P. J., Caulfield, M., Eriksson, M., Grundy, S. M., Kastelein, J. J., Komajda, M., Lopez-Sendon, J., Mosca, L., Tardif, J. C., Waters, D. D., Shear, C. L., Revkin, J. H., Buhr, K. A., Fisher, M. R., Tall, A. R., and Brewer, B. (2007) *N. Engl. J. Med.* **357,** 2109–2122
15. Davidson, W. S., and Thompson, T. B. (2007) *J. Biol. Chem.* **282,** 22249–22253
16. Thomas, M. J., Bhat, S., and Sorci-Thomas, M. G. (2008) *J. Lipid Res.* **49,** 1875–1883
17. Phillips, J. C., Wriggers, W., Li, Z., Jonas, A., and Schulten, K. (1997) *Biophys. J.* **73,** 2337–2346
18. Segrest, J. P., Jones, M. K., Klon, A. E., Sheldahl, C. J., Hellinger, M., De Loof, H., and Harvey, S. C. (1999) *J. Biol. Chem.* **274,** 31755–31758
19. Koppaka, V., Silvestro, L., Engler, J. A., Brouillette, C. G., and Axelsen, P. H. (1999) *J. Biol. Chem.* **274,** 14541–14544
20. Bhat, S., Sorci-Thomas, M. G., Alexander, E. T., Samuel, M. P., and Thomas, M. J. (2005) *J. Biol. Chem.* **280,** 33015–33025
21. Martin, D. D., Budamagunta, M. S., Ryan, R. O., Voss, J. C., and Oda, M. N. (2006) *J. Biol. Chem.* **281,** 20418–20426
22. Maiorano, J. N., Jandacek, R. J., Horace, E. M., and Davidson, W. S. (2004) *Biochemistry* **43,** 11717–11726
23. Wu, Z., Wagner, M. A., Zheng, L., Parks, J. S., Shy, J. M., 3rd, Smith, J. D., Gogonea, V., and Hazen, S. L. (2007) *Nat. Struct. Mol. Biol.* **14,** 861–868
24. Gingras, A. R., Bate, N., Goult, B. T., Hazelwood, L., Canestrelli, I., Grossmann, J. G., Liu, H., Putz, N. S., Roberts, G. C., Volkmann, N., Hanein, D., Barsukov, I. L., and Critchley, D. R. (2008) *EMBO J.* **27,** 458–469
25. Radford, S. E., Dobson, C. M., and Evans, P. A. (1992) *Nature* **358,** 302–307
26. Cowieson, N. P., Kobe, B., and Martin, J. L. (2008) *Curr. Opin. Struct. Biol.* **18,** 617–622
27. Fleishman, S. J., Unger, V. M., and Ben-Tal, N. (2006) *Trends Biochem. Sci.* **31,** 106–113
28. Shaw, J. A., Bobik, A., Murphy, A., Kanellakis, P., Blombery, P., Mukhamedova, N., Woollard, K., Lyon, S., Sviridov, D., and Dart, A. M. (2008) *Circ. Res.* **103,** 1084–1091
29. Imaizumi, S., Miura, S., Nakamura, K., Kiya, Y., Uehara, Y., Zhang, B., Matsuo, Y., Urata, H., Ideishi, M., Rye, K. A., Sata, M., and Saku, K. (2008) *J. Am. Coll. Cardiol.* **51,** 1604–1612
30. Ibanez, B., Vilahur, G., Cimmino, G., Speidl, W. S., Pinero, A., Choi, B. G., Zafar, M. U., Santos-Gallego, C. G., Krause, B., Badimon, L., Fuster, V., and Badimon, J. J. (2008) *J. Am. Coll. Cardiol.* **51,** 1104–1109
31. Duong, P. T., Collins, H. L., Nickel, M., Lund-Katz, S., Rothblat, G. H., and Phillips, M. C. (2006) *J. Lipid Res.* **47,** 832–843
32. Matz, C. E., and Jonas, A. (1982) *J. Biol. Chem.* **257,** 4535–4540
33. Peng, D. Q., Wu, Z., Brubaker, G., Zheng, L., Settle, M., Gross, E., Kinter, M., Hazen, S. L., and Smith, J. D. (2005) *J. Biol. Chem.* **280,** 33775–33784
34. Meilleur, F., Contzen, J., Myles, D. A., and Jung, C. (2004) *Biochemistry* **43,** 8744–8753
35. Artero, J. B., Härtlein, M., McSweeney, S., and Timmins, P. (2005) *Acta Crystallogr. D Biol. Crystallogr.* **61,** 1541–1549
36. Niemann, H. H., Petoukhov, M. V., Härtlein, M., Moulin, M., Gherardi, E., Timmins, P., Heinz, D. W., and Svergun, D. I. (2008) *J. Mol. Biol.* **377,** 489–500
37. Baker, P. W., Rye, K. A., Gamble, J. R., Vadas, M. A., and Barter, P. J. (2000) *J. Lipid Res.* **41,** 1261–1267
38. Andrade, M. A., Chacón, P., Merelo, J. J., and Morán, F. (1993) *Protein Eng.*

6, 383–390
39. Jin, L., Shieh, J. J., Grabbe, E., Adimoolam, S., Durbin, D., and Jonas, A. (1999) *Biochemistry* **38,** 15659–15665
40. Bolton, A. E., and Hunter, W. M. (1973) *Biochem. J.* **133,** 529–539
41. Gu, X., Trigatti, B., Xu, S., Acton, S., Babitt, J., and Krieger, M. (1998) *J. Biol. Chem.* **273,** 26338–26348
42. Johs, A., Hammel, M., Waldner, I., May, R. P., Laggner, P., and Prassl, R. (2006) *J. Biol. Chem.* **281,** 19732–19739
43. Guinier, A. (1939) *Ann. Phys.* **12,** 161–237
44. Zaccaï, G., and Jacrot, B. (1983) *Annu. Rev. Biophys. Bioeng.* **12,** 139–157
45. Svergun, D. I. (1999) *Biophys. J.* **76,** 2879–2886
46. Konarev, P. V., Sokolova, A. V., Koch M. H. J., and Svergun, D. I. (2003) *J. Appl. Crystallogr.* 1277–1282
47. Petoukhov, M. K., P. V., Kikhney, A. G., and Svergun, D. (2007) *J. Appl. Crystallogr.* **40,** S223–S228
48. Silva, R. A., Hilliard, G. M., Li, L., Segrest, J. P., and Davidson, W. S. (2005) *Biochemistry* **44,** 8600–8607
49. Li, H. H., Lyles, D. S., Pan, W., Alexander, E., Thomas, M. J., and Sorci-Thomas, M. G. (2002) *J. Biol. Chem.* **277,** 39093–39101
50. Miranker, A., Robinson, C. V., Radford, S. E., Aplin, R. T., and Dobson, C. M. (1993) *Science* **262,** 896–900
51. Chung, E. W., Nettleton, E. J., Morgan, C. J., Gross, M., Miranker, A., Radford, S. E., Dobson, C. M., and Robinson, C. V. (1997) *Protein Sci.* **6,** 1316–1324
52. Guex, N., and Peitsch, M. C. (1997) *Electrophoresis* **18,** 2714–2723
53. Sali, A., and Blundell, T. L. (1993) *J. Mol. Biol.* **234,** 779–815
54. Merzel, F., and Smith, J. C. (2002) *Acta Crystallogr. D Biol. Crystallogr.* **58,** 242–249
55. Svergun, D. I., Richard, S., Koch, M. H., Sayers, Z., Kuprin, S., and Zaccai, G. (1998) *Proc. Natl. Acad. Sci. U.S.A.* **95,** 2267–2272
56. Jorgensen, W. L., and Tirado-Rives, J. (1988) *J. Am. Chem. Soc.* **110,** 1657–1666
57. Lindahl, E., Hess, B., and van der Spoel, D. (2001) *J. Mol. Mod.* **7,** 306
58. Serdyuk, I. N., Zaccai, N. R., and Zaccai, J. (eds) (2007) *Methods in Molecular Biophysics*, p. 776, Cambridge University Press, Cambridge, UK
59. Pardon, J. F., Worcester, D. L., Wooley, J. C., Cotter, R. I., Lilley, D. M., and Richards, R. M. (1977) *Nucleic Acids Res.* **4,** 3199–3214
60. Ramakrishnan, V. (1986) *Science* **231,** 1562–1564
61. May, R. P., Nowotny, V., Nowotny, P., Voss, H., and Nierhaus, K. H. (1992) *EMBO J.* **11,** 373–378
62. Willumeit, R., Diedrich, G., Forthmann, S., Beckmann, J., May, R. P., Stuhrmann, H. B., and Nierhaus, K. H. (2001) *Biochim. Biophys. Acta* **1520,** 7–20
63. Catte, A., Patterson, J. C., Jones, M. K., Jerome, W. G., Bashtovyy, D., Su, Z., Gu, F., Chen, J., Aliste, M. P., Harvey, S. C., Li, L., Weinstein, G., and Segrest, J. P. (2006) *Biophys. J.* **90,** 4345–4360
64. Zhu, H. L., and Atkinson, D. (2004) *Biochemistry* **43,** 13156–13164
65. Rogers, D. P., Roberts, L. M., Lebowitz, J., Engler, J. A., and Brouillette, C. G. (1998) *Biochemistry* **37,** 945–955
66. Atkinson, D., Small, D. M., and Shipley, G. G. (1980) *Ann. N.Y. Acad. Sci.* **348,** 284–298
67. Shih, A. Y., Arkhipov, A., Freddolino, P. L., Sligar, S. G., and Schulten, K. (2007) *J. Phys. Chem. B* **111,** 11095–11104
68. Denisov, I. G., Grinkova, Y. V., Lazarides, A. A., and Sligar, S. G. (2004) *J. Am. Chem. Soc.* **126,** 3477–3487
69. Peters-Libeu, C. A., Newhouse, Y., Hall, S. C., Witkowska, H. E., and Weisgraber, K. H. (2007) *J. Lipid Res.* **48,** 1035–1044
70. Borhani, D. W., Rogers, D. P., Engler, J. A., and Brouillette, C. G. (1997) *Proc. Natl. Acad. Sci. U.S.A.* **94,** 12291–12296
71. Tardif, J. C., Grégoire, J., L'Allier, P. L., Ibrahim, R., Lespérance, J., Heinonen, T. M., Kouz, S., Berry, C., Basser, R., Lavoie, M. A., Guertin, M. C., and Rodés-Cabau, J. (2007) *JAMA* **297,** 1675–1682
72. Nicholls, S. J., Cutri, B., Worthley, S. G., Kee, P., Rye, K. A., Bao, S., and Barter, P. J. (2005) *Arterioscler. Thromb. Vasc. Biol.* **25,** 2416–2421
73. Ajees, A. A., Anantharamaiah, G. M., Mishra, V. K., Hussain, M. M., and Murthy, H. M. (2006) *Proc. Natl. Acad. Sci. U.S.A.* **103,** 2126–2131
74. Peng, D. Q., Brubaker, G., Wu, Z., Zheng, L., Willard, B., Kinter, M., Hazen, S. L., and Smith, J. D. (2008) *Arterioscler. Thromb. Vasc. Biol.* **28,** 2063–2070
75. Shih, A. Y., Sligar, S. G., and Schulten, K. (2008) *Biophys. J.* **94,** L87–89
76. Rye, K. A., Garrety, K. H., and Barter, P. J. (1992) *J. Lipid Res.* **33,** 215–224
77. Alexander, E. T., Bhat, S., Thomas, M. J., Weinberg, R. B., Cook, V. R., Bharadwaj, M. S., and Sorci-Thomas, M. (2005) *Biochemistry* **44,** 5409–5419
78. Koukos, G., Chroni, A., Duka, A., Kardassis, D., and Zannis, V. I. (2007) *Biochem. J.* **406,** 167–174
79. Black, S. D., and Mould, D. R. (1991) *Anal. Biochem.* **193,** 72–82
80. Li, H. H., Thomas, M. J., Pan, W., Alexander, E., Samuel, M., and Sorci-Thomas, M. G. (2001) *J. Lipid Res.* **42,** 2084–2091
81. Bhat, S., Sorci-Thomas, M. G., Tuladhar, R., Samuel, M. P., and Thomas, M. J. (2007) *Biochemistry* **46,** 7811–7821

Double Superhelix Model of High Density Lipoprotein

Zhiping Wu, Valentin Gogonea, Xavier Lee, Matthew A. Wagner, Xin-Min Li, Ying Huang, Arundhati Undurti, Roland P. May, Michael Haertlein, Martine Moulin, Irina Gutsche, Giuseppe Zaccai, Joseph A. DiDonato and Stanley L. Hazen

J. Biol. Chem. 2009, 284:36605-36619.
doi: 10.1074/jbc.M109.039537 originally published online October 7, 2009
